Highlights on the reversible nonpolar-to-polar P3121–P31 phase transition at low temperature in NaLa(SO4)2×H2O: mechanism and piezoelectric properties

H Azeroual, J-L Bantignies, D Maurin, D Granier, J Haines, O Cambon, P Hermet

PCCP
Physical Chemistry Chemical Physics

Accepted Manuscript

This article can be cited before page numbers have been issued, to do this please use: H. Azeroual, J. Bantignies, D. Maurin, D. Granier, J. Haines, O. Cambon and P. Hermet, *Phys. Chem. Chem. Phys.*, 2023, DOI: 10.1039/D3CP00587A.

View Article Online
DOI: 10.1039/D3CP00587A

Journal Name

ARTICLE TYPE

Cite this: DOI: 00.0000/xxxxxxxxxx

Highlights on the reversible nonpolar-to-polar $P3_121$-$P3_1$ phase transition at low temperature in $NaLa(SO_4)_2.H_2O$: mechanism and piezoelectric properties†

H. Azeroual,[a] J.-L. Bantignies,[b] D. Maurin,[b] D. Granier,[a] J. Haines,[a] O. Cambon,[a] and P. Hermet[a‡]

Received Date
Accepted Date

DOI: 00.0000/xxxxxxxxxx

We report the existence in $NaLa(SO_4)_2.H_2O$ of a displacive phase transition under 200 K from the nonpolar $P3_121$ to the polar $P3_1$ space group. This phase transition was predicted by density functional theory based calculations and experimentally confirmed from infrared spectroscopy and x-ray diffraction. The A_2 polar irreducible representation is the primary order parameter. The structural water and hydrogen bonding are the mechanism driving the phase transition. The piezoelectric properties of this new $P3_1$ phase have been investigated by first principles based calculations. The highest piezoelectric-strain constants in the zero Kelvin limit are predicted for the d_{12} and d_{41} elements with values about 3.4 pC/N. This compound could be interesting as piezoelectric actuator for cryogenic applications.

1 Introduction

α-Quartz crystallizes in the trigonal $P3_121$ (or $P3_221$) space group with corner-sharing SiO_4 tetrahedra aligned along the c-axis. This compound is widely involved in piezoelectric applications despite a small electromechanical coupling ($k \sim 8\%$)[1] and piezoelectric-strain constant ($d_{11} = 2.5$ pC/N)[2]. Furthermore, the existence of a phase transition near 846 K to a weakly piezoelectric structure (β-quartz)[3,4] restricts its area of applications. This is the reason why considerable efforts have been devoted to find analogous materials with better intrinsic properties. In this research, the 32-point group has been intensively investigated. For example, in contrast to α-quartz where all tetrahedra are identical, $M^{III}X^{V}O_4$ (M = B, Ga, Al, Fe and X = P, As) are described as a helical chain of $M^{III}O_4$ and $X^{V}O_4$ tetrahedra alternatively linked along the c-axis[5–12]. Most of these homeotypes present a higher electromechanical coupling than α-quartz and can reach up to[10,13] $k_{26} \sim 22\%$ in $GaAsO_4$ without undergoing any phase transition until its decomposition temperature (1303 K)[9,14]. Langatate or langasite are compounds with the $A_3BC_3D_2O_{14}$ general formula and adopt to the P321 space group[15]. They can be described as a framework formed by five tetrahedra (three CO_4 and two DO_4), one BO_6 octahedron, and A is a decahedral site coordinated by eight oxygen atoms. In particular, the $La_3Ga_5SiO_{14}$ langasite has a piezoelectric-strain constant ($d_{11} \sim$-6.5 pC/N)[16] 2.5 times higher than in α-quartz, an electromechanical coupling coefficient of $k_{26} = 13.4\%$[17] and no structural phase transition between room temperature and its melting point at 1470°C[18]. More recently, first-principles-based calculations predicted in $BaZnO_2$ a piezoelectric-strain constant and an electromechanical coupling coefficient of[19]: $d_{11} = 11.84$ pC/N and $k_{11} = 35.7\%$. This compound shares the same space group as α-quartz. However, the screw axis of this trigonal unit cell is defined by the arrangement of corner-sharing ZnO_4 tetrahedra around the barium atom, which is located in a distorted 8-fold oxygen atom coordination[20].

In this context, we are interested in the $NaLn(SO_4)_2.H_2O$ family, with Ln = La–Yb, as promising piezoelectric materials. The crystal structure of the compounds within this family have been reported in the literature at room temperature[21–29]. All structures belong to the $P3_121$ space group or in its enantiomorphic analog $P3_221$. The structure consists of LaO_9 tricapped trigonal prisms, NaO_8 square-antiprisms and SO_4 tetrahedra polyhedra. The structural water is helically placed along the 3_1 axis[24,26]. To our knowledge, there is no experimental or theoretical study of the piezoelectric properties devoted to this family. Our study naturally began with the simpliest compound within this family, $NaLa(SO_4)_2.H_2O$, since it is the only one that does not have magnetic properties. However, the calculation of its piezoelectric properties was not possible because of unstable phonon modes at the zone-center.

In this article, we report the existence and the mechanism in $NaLa(SO_4)_2.H_2O$ of a displacive phase transition at 200 K from

[a]ICGM, Univ. Montpellier, CNRS, ENSCM, Montpellier, France
[b]Laboratoire Charles Coulomb (L2C), CNRS, University of Montpellier, France
† Electronic Supplementary Information (ESI) available. See DOI: 00.0000/00000000.
‡ Corresponding author. E-mail: patrick.hermet@umontpellier.fr

View Article Online
DOI: 10.1039/D3CP00587A

the nonpolar $P3_121$ to the polar $P3_1$ space groups. The discussion of this article is organized in four parts. The first part discusses the structure and the lattice dynamics of $NaLa(SO_4)_2.H_2O$ in the $P3_121$ space group. Although our calculation reproduced quite well the experimental infrared spectrum, they revealed three unstable polar phonons suggesting a displacive phase transition at low temperature toward a $P3_1$ subgroup. The used methodology to identify the polar $P3_1$ space group and the mechanism of the $P3_121$-$P3_1$ phase transtion is explained from symmetry-adapted distortion modes in the second part. This approach involves describing the $P3_1$ structure as arising from the $P3_121$ structure with one (or more) static symmetry-breaking structural distortion(s). The third part is purely experimental and confirms, independently with respect to our calculations, the DFT predictions. We determined the temperature where the phase transition takes place by infrared spectroscopy and x-ray diffraction performed below this temperature on single crystal identified the $P3_1$ space group. The last part is devoted to the piezoelectric properties of this new $P3_1$ phase.

2 Synthesis and Experimental setup

The synthesis and the crystal growth process of $NaLa(SO_4)_2.H_2O$ have already been detailed in ref.[30]. A suitable single crystal ($202\times201\times150$ μm) was mounted on a cryoloop and the crystal structure was determined by x-ray diffraction using a Bruker 4-circle D8 Venture diffractometer with a PHOTON II area detector, using Mo K_α radiation (0.71073 Å) from an Incoatec IμS 3.0 microsource with focusing mirrors operating at 50 kV and 1 mA. The data collection was performed at 100 K using APEX4 sofware and the structure was solved by direct methods. A first determination of the structure by using SHELXT 2018/2 sofware led to a bad solution with $R1 = 13.7\%$. By introducing an inversion twin law defined by the (0 1 0, 1 0 0, 0 0 -1) matrix, the refinement by using SHELXL 2019/1 software resulted in a good structural model ($R1 = 1.5\%$) with the $P3_1$ space group. The absorption correction type is multi-scan performed by SADABS-2016/2 - Bruker AXS area detector scaling.

Infrared measurements were carried out in the far-infrared (50–600 cm^{-1}) and mid-infrared (600–4000 cm^{-1}) regions. We used a Bruker IFS 66V Fourier transform spectrometer using a black body source and two different beamsplitters covered the whole spectral region: bromide potassium (mid-infrared) and Ge-coated (far-infrared). A Si-bolometer detector cooled at 4 K was used to probe the far-infrared domain with extra sensitivity and a N_2-cooled MCT (mercury cadmium telluride) detector was used in the mid-infrared domain. The spectral resolution was 2 cm^{-1} and 64 scans were accumulated for each spectrum. The measurements were performed in the 25–295 K range using a cold finger helium cryostat. The sample was gently ground with polyethylene (resp. bromide potassium) powder according to the 1/70 (resp. 1/300) mass ratio and compressed under 8 tons to form an isotropic pellet of 12 mm diameter.

3 Computational details

Calculations were performed within the density functional theory (DFT) and using a plane-wave pseudopotentials method as implemented in the ABINIT package[31]. The exchange-correlation energy functional is evaluated using the generalized gradient approximation (GGA) parametrized by Perdew, Burke and Ernzerhof (PBE)[32]. The all-electron potentials are replaced by norm-conserving pseudopotentials generated according to the Troullier-Martins scheme. Na($2s^2$, $2p^6$, $3s^1$), La($5s^2$, $5p^6$, $5d^1$, $6s^2$), S($3s^2$, $3p^4$), O($2s^2$, $2p^4$) and H($1s^1$)-electrons are considered as valence states. The electronic wave functions are expanded in plane-waves up to a kinetic energy cutoff of 67 Ha and integrals over the Brillouin zone are approximated by sums over a $6\times6\times6$ mesh of special k-points according to the Monkhorst-Pack scheme[33]. These k-point sampling and kinetic energy cutoff give converged results. Lattice parameters and atomic positions were fully relaxed using a Broyden-Fletcher-Goldfarb-Shanno algorithm until the maximum stresses and residual forces were less than 7×10^{-4} GPa and 6×10^{-6} Ha/Bohr, respectively. Dynamical matrix at the zone center, Born effective charges, dielectric, elastic and piezoelectric tensors have been calculated within a variational approach to density functional perturbation theory. Infrared absorbance spectra were calculated according to the formalism described in ref.[34]. In our calculations, the Cartesian x (resp. z) axes are collinear to the a (resp. c) crystal directions. The y-axis is the free axis.

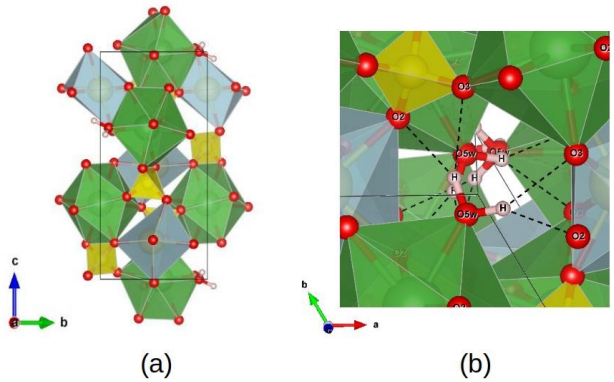

Fig. 1 (a) Relaxed crystal structure of $NaLa(SO_4)_2.H_2O$ in the $P3_121$ space group along the a-axis. This representation highligths the three different polyhedra. The polyhedra centered on Na-, La- and S-atoms are displayed in cyan, green and yellow, respectively. The oxygen and hydrogen atoms are in red and white balls, respectively. (b) Schema of the bifurcated hydrogen bonding in the structure.

4 Results and discussion

4.1 Structure and lattice dynamics of the $P3_121$ phase

In 1994, Blackburn *et al.*[26] reported for the first time the crystal structure of $NaLa(SO_4)_2.H_2O$ at room temperature using X-ray diffraction. However, their sructure was not fully resolved as the position of the water molecules remained uncertain. In 2005, Perles *et al.*[24] located the hydrogen atoms from the water molecule using a difference Fourier analysis and included them in the refinement process. In agreement with Blackburn *et al.*[26], they reported that $NaLa(SO_4)_2.H_2O$ crystallizes at room temperature in

View Article Online
DOI: 10.1039/D3CP00587A

the acentric trigonal system with the $P3_121$ (D_3^4) space group and the lattice parameters a =7.0538(5) and c =12.9625(14) Å. The asymmetric unit contains 9 atoms (see Table 1). All atoms occupy the general 6*c* Wyckoff position with C_1 site symmetry except lanthanum (3*a*), sodium (3*b*) and water oxygen (3*a*) atoms which occupy special Wyckoff positions with C_2 site symmetry.

Recently, the crystal structure of $NaLa(SO_4)_2.H_2O$ has also been investigated by our group using x-ray diffraction to understand the dehydration process at high temperature[30]. Similarly with this study, the consideration of hydrogen atoms in the structural model does not improve our refinement. Results of our refinement, reported in Table 1 at room temperature, are consistent with those of Perles *et al.*[24] as shown by the small lattice distortion (η =0.02%) and similarity factor[35] (Δ =0.2%)[36] calculated without hydrogen atoms. The higher discrepancy between the two experimental structure listed in Table 1 is observed for the water oxygen atom (O_{5w}) with an atomic displacement of (-0.0055, -0.0055, 0.0000) in reduced units. In the structure proposed by Perles *et al.*[24], the position of the O_{5w} and hydrogen atoms are not very accurate considering their high standard deviation values. In our refinement, the position of the atoms are well determined with a smaller standard deviation. This is the reason why this structure was used as starting point in our DFT-based calculations.

All the studies report that the $NaLa(SO_4)_2.H_2O$ structure at room temperature can be seen as built from LaO_9 tricapped trigonal prisms, NaO_8 square-antiprisms and SO_4 tetrahedra polyhedra (Figure 1(a)). The lanthanum is coordinated with six sulfate groups and one water molecule. Over the six sulfate groups, two share their edges by two oxygen atoms and the other four share their corners by one oxygen atom. Sodium is coordinated by six sulfate groups (four are corner-sharing and two are edge-sharing). Sulfur atoms are in a slightly irregular tetrahedron environment. The water molecules are helicaly placed along the 3_1 axis. Each hydrogen atom form a bifurcated hydrogen bond with a sulphate oxygen atom: H...O_2 and H...O_3 (see Figure 1(b)).

Relaxation of the $NaLa(SO_4)_2.H_2O$ structure has been performed by DFT and results are listed in Table 1. We observe a dilatation of the calculated unit cell about 1.4% along the three directions, leading to a calculated volume 4.2% higher than in the experiments. These trends and these relative errors are commonly observed with the PBE functional. The calculated atomic positions show similar agreement with respect to the two sets of experimental data. The similitude factor between our calculation and the atomic positions from Perles *et al.*[24] is Δ =0.015 including hydrogen atoms. Without the hydrogens in the calculation of Δ, we get Δ =0.010 with the structure from Perles *et al.* and Δ =0.009 with the structure from Azeroual *et al.*. The calculated average of the La-O, Na-O and S-O distances are slightly overestimated between 1.0 and 1.6% in comparison with the experimental ones. The calculated position of the water oxygen (O_{5w}) is in excellent agreement with the experimental refinement from Azeroual *et al.* and shows a difference of (-0.0018, -0.0018, 0.0000) in reduced units against (-0.0073, -0.0073, 0.0000) for the O_{5w} position refined by Perles *et al.*. The calculated position of hydrogen atoms gives the higher difference between our calculation and

		Experiment[24] [300 K]	Experiment[30] [300 K]	Calculation [0 K]
Lattice parameters				
a [Å]		7.0538(5)	7.0516(1)	7.1470
c [Å]		12.9625(14)	12.9587(2)	13.1405
c/a		1.8377	1.8377	1.8403
Ω_0 [Å^3]		558.55	558.042(18)	581.295
Atomic positions (reduced units)				
La	x	0.5674(1)	0.5674(1)	0.5643
	y	0.5674(1)	0.5674(1)	0.5643
	z	0.0000	0.0000	0.0000
O_1	x	0.4956(9)	0.4969(1)	0.4925
	y	0.3630(9)	0.3635(1)	0.3583
	z	0.8257(3)	0.8254(1)	0.8275
O_2	x	0.6109(7)	0.6103(2)	0.6046
	y	0.7406(7)	0.7398(1)	0.7339
	z	0.8184(3)	0.8182(8)	0.8210
O_3	x	0.4090(8)	0.4085(2)	0.4101
	y	0.1637(8)	0.1627(2)	0.1621
	z	0.0262(4)	0.0260(1)	0.0297
O_4	x	0.4975(9)	0.4987(2)	0.5028
	y	0.8821(9)	0.8815(2)	0.8832
	z	0.0137(3)	0.0135(1)	0.0155
S	x	0.5600(3)	0.5599(1)	0.5556
	y	0.5474(3)	0.5473(1)	0.5425
	z	0.7533(1)	0.7533(1)	0.7559
O_{5w}	x	0.9302(14)	0.9247(3)	0.9229
	y	0.9302(14)	0.9247(3)	0.9229
	z	0.0000	0.0000	0.0000
Na	x	0.0000	0.0000	0.0000
	y	0.4700(6)	0.4693(1)	0.4784
	z	1/6	1/6	1/6
H	x	0.049(17)	-	0.0589
	y	0.93(2)	-	0.9523
	z	0.056(7)	-	0.0303
Volume of polyhedra P[X] (Å^3)				
P[Na]		28.050	28.014	29.441
P[La]		32.937	32.737	33.753
P[S]		1.643	1.641	1.701
Mean distances (Å)				
<Na-O>		2.590	2.589	2.633
<La-O>		2.553	2.547	2.570
<S-O>		1.475	1.474	1.492
Hydrogen bond distances (Å): O_{5w} – H ⋯ O				
O_{5w} ... O_2		3.228(5)	3.240(16)	3.442
O_{5w} ... O_3		2.945(9)	2.974(3)	3.041
H ... O_2		2.1(1)	-	2.460
H ... O_3		2.3(1)	-	2.188

Table 1 Structural parameters in the $P3_121$ phase of $NaLa(SO_4)_2.H_2O$. P(X) is the polyhedra centered on the X-atom.

View Article Online
DOI: 10.1039/D3CP00587A

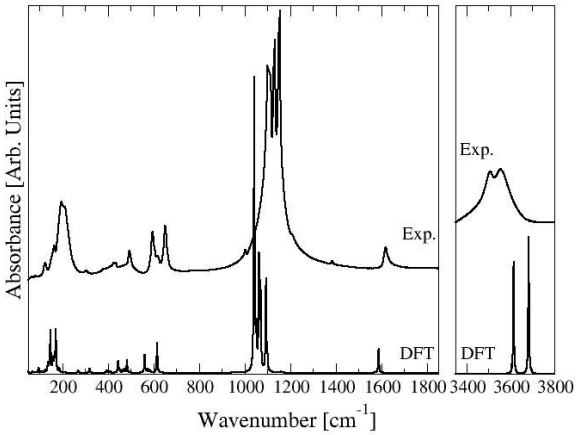

Fig. 2 Experimental infrared absorbance spectrum of $NaLa(SO_4)_2.H_2O$ in the $P3_121$ phase (295 K) and the corresponding calculated spectrum (0 K). The calculated spectrum is displayed using a Lorentzian line shape and a constant linewidth fixed at 2 cm^{-1}.

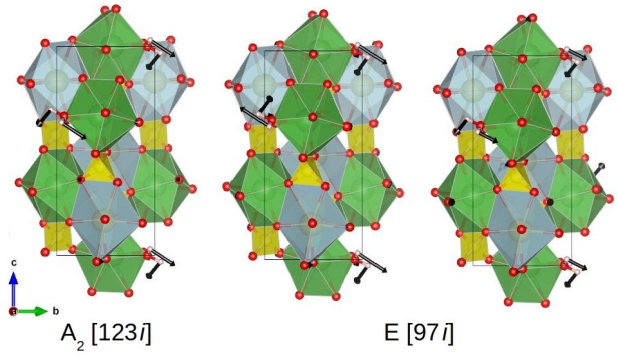

Fig. 3 Eigendisplacement vector of the three unstable modes in $NaLa(SO_4)_2.H_2O$ with the $P3_121$ space group. The color code is the same than in Figure 1. The frequency in cm^{-1} is between brackets.

the experiment where a difference of (0.0099, 0.0223, -0.0257) in reduced unit can be observed.

Group theory predicts that each of the six (resp. three) atoms of the $NaLa(SO_4)_2.H_2O$ asymmetric unit located on the C_1-site (resp. C_2-site) contributes to: $3A_1 \oplus 3A_2 \oplus 6E$ (resp. $A_1 \oplus 2A_2 \oplus 3E$). Thus, the corresponding irreducible representation of the acoustic (Γ_{acc}) and optical (Γ_{opt}) vibrational modes at the zone-center (Γ-point) is: $\Gamma_{acc} = A_2 \oplus E$ and $\Gamma_{opt} = 21A_1 \oplus 23A_2 \oplus 44E$. The E representation is simultaneously infrared and Raman active whereas the A_2 (resp. A_1) representation is only infrared (resp. Raman) active.

The experimental infrared spectrum measured at room temperature using an absorbance configuration is reported in Figure 2 within the 50-3800 cm^{-1} range (see Figure S1 in ESI for the 1800–3000 cm^{-1} range). This spectrum has been normalized on the band located at 595 cm^{-1} which is common to the far- and mid-infrared domain. The DFT infrared spectrum calculated at 0 K is also reported in this figure. The band width cannot be calculated within the framework of the harmonic approximation and is arbitrarily fixed at 2 cm^{-1}. The number of calculated bands, their frequency position and their relative intensity are in good agreement with the experiment. We just observe an inversion in the relative intensity of the triplet about 1100 cm^{-1}. The slight underestimation (except for the couple of bands around 3600 cm^{-1}) in the calculated frequencies could be related to the difference of temperature between the calculation and the experiment.

Mode assignments (given following Herzberg's notation[37]) are carried out from the analysis of the eigendisplacement vectors obtained by diagonalization of the dynamical matrix. The experimental spectrum can be divided into three regions. The first region (3800–1500 cm^{-1}) is dominated by motions of the water molecules. The bands centered at 3558 and 3508 cm^{-1} are assigned to the O-H asymmetric (ν_3) and symmetric (ν_1) stretching vibrations. The band at 1619 cm^{-1} is ascribed to the H-O-H bending deformation (ν_2). The shape and the position of the stretching bands show that water molecules have the same environment and form hydrogen bonds of weak intensity. Thus, we have one type of water molecules which is consistent with the chemical formula. Combination bands of sulfate groups can also be observed within this domain (see Figure S1 in ESI). The second region (1500–400 cm^{-1}) is dominated by the motions of sulphate groups. The intense triplet of bands about 1132 cm^{-1} dominates the infrared spectrum and corresponds to the stretching modes. The bands at 1150 and 1130 cm^{-1} are assigned to asymmetric stretching (ν_3) while the remaining one is the symmetric stretching (ν_1). The bending modes of sulphate groups are observed between 600 and 400 cm^{-1} and bands have medium intensity. The couple of bands around 620 cm^{-1} are assigned to antisymmetric bending vibrations (ν_4) whereas the one around 460 cm^{-1} is the symmetric bendings (ν_2). The last region (400–50 cm^{-1}) is complex to analyze because this is the domain where external vibrations of water, sulfate and LaO_9 appears. This region is dominated by an intense band at 206 cm^{-1} assigned to deformations of water molecules combined with deformation of NaO_8 and LaO_9 polyhedra. The remaining bands have low intensity. The band about 305 cm^{-1} is a wagging of water molecules. The libration of sulphate groups are evidenced about 110 cm^{-1}.

Below 50 cm^{-1}, our calulations reveal two distinct unstable zone-center modes, suggesting that $NaLa(SO_4)_2.H_2O$ undergoes a displacive phase transition at low temperature to a subgroup of the $P3_121$ space group. The mode with the largest imaginary frequency ($123i$ cm^{-1}) belongs to the A_2 irreducible representation whereas the other mode belongs to the E representation and has an imaginary frequency at $97i$ cm^{-1}. The eigendisplacement vectors of these three modes correspond to a twisting of water molecules (Figure 3). From symmetry considerations, the number of potential subgroups can only be three and are: trigonal $P3_1$, monoclinic C2 or triclinic P1. Indeed, the $P3_1$ phase can be obtained from the condensation of the A_2 unstable mode in the $P3_121$ phase whereas the C2 or P1 phase can be obtained from the condensation of the unstable E mode in the $P3_121$ phase. In the

View Article Online
DOI: 10.1039/D3CP00587A

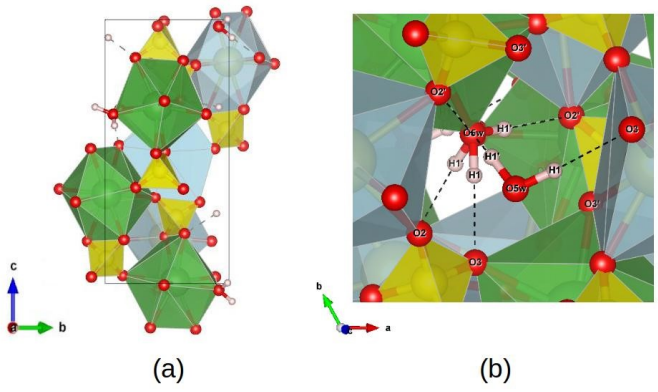

Fig. 4 (a) Relaxed crystal structure of $NaLa(SO_4)_2.H_2O$ in the $P3_1$ space group along the a-axis. (b) Schema of the hydrogen bonding in the structure. The same color code than in Figure 1 is used.

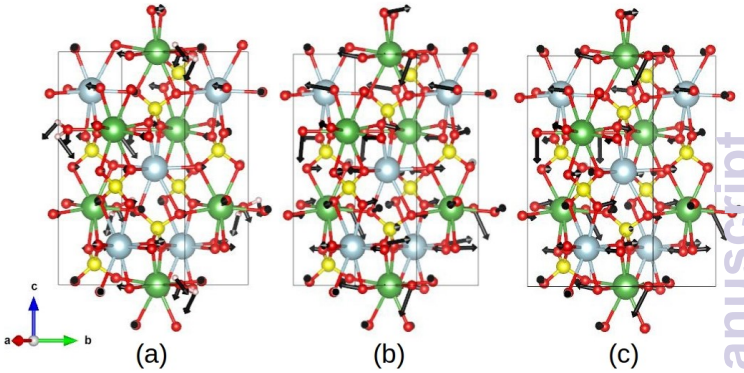

Fig. 5 Distortion vector between the $P3_1$ and the $P3_121$ phases in $NaLa(SO_4)_2.H_2O$. This vector has been calculated from the DFT structures (a), the DFT structures whithout hydrogen atoms (b) and our experimental structures for which hydrogen atoms could not be determined by x-ray diffraction (c). The Na-, La-, S- and O-atoms are displayed in cyan, green, yellow and red, respectively.

case of the condensation of the E-mode, we have two possibilities because this representation is twofold degenerate. In contrast to the the parent $P3_121$ group, these three subgroups belong to pyroelectric groups. In addition, the unit cell of these low symmetry structures is not enlarged with respect to the parent structure ($P3_121$ phase) as the instablilities are at the zone center. Only the number of atoms in the asymmetric unit can change between these structures.

4.2 Prediction of the $P3_121$-$P3_1$ phase transition and mechanism

Identification. The relaxed lattice parameters of the $P3_1$, C2 and P1 phases are listed in Table 2 with their electronic energy relative to the $P3_121$ phase. As expected, these three phases are more stable than the $P3_121$ phase and their primitive unit cell volume (Ω_0 =574–577 Å^3) is very similar to that calculated for the $P3_121$ phase ($\Omega_0 \sim$581 Å^3). The energy of the C2 and the $P3_121$ phases differ by -25.04 meV. The P1 phase is more stable than the C2 phase by about the same amount of energy. The lowest energy configuration corresponds to the trigonal $P3_1$ phase with a decrease of 113 meV (resp. 87.9 meV) with respect to the $P3_121$ (resp. C_2) phase. We checked that this tendency should be preserved even under small variation of the unit cell volume. Further phonon calculations at the zone-center do not reveal any unstable mode, identifying this $P3_1$ phase as potential ground state at low temperature.

The structure of $NaLa(SO_4)_2.H_2O$ in the $P3_1$ phase (Table 2) is similar to that in the $P3_121$ phase (Table 1). The lattice parameters are slightly smaller (-0.5% for a and -0.2% for c), yielding an underestimation of -1.2% for the unit cell volume. The c/a ratio is preserved during the phase transition. The coordination of the lanthanum (9), sodium (8) and sulfur (4) with oxygen atoms remain unchanged (Figure 4a). The water molecules are also along the 3_1 screw axis with the water oxygen atom (O_{5w}) coordinated to the lanthanum. However, the loss of the twofold symmetry leads each atoms at the 6c Wyckoff positions in the $P3_121$ phase to split into two in the $P3_1$ phase. Thus, the sulphur atoms can be separated into types S_1 and $S_{1'}$ in the $P3_1$ phase which form two slightly different sulphate units. The four inequivalent oxygen atoms bonded to S_1 (resp. $S_{1'}$) are labeled as O_1, O_2, O_3 and O_4 (resp. $O_{1'}$, $O_{2'}$, $O_{3'}$ and $O_{4'}$). The La-O, Na-O and S-O intrapolyhedral mean distances do not evolve with respect to the $P3_121$ phase. A similar observation can be made on the volume of the polyhedra. In contrast, we observe that the hydrogen bonding is strengthened in the $P3_1$ phase as the different O...H and O_{5w}...O distances are significantly shorter (Tables 1 and 3): the calculated O...H (resp. O_{5w}...O) distances are $\sim$ 2.0 Å (resp. 2.9–3.0 Å) in the $P3_1$ phase against 2.2–2.5 Å (resp. 3.0–3.4 Å) in the $P3_121$ phase. However, the hydrogen bond is no longer bifurcated in the $P3_1$ phase as the H_1-$O_{3'}$, H_1-O_2 and $H_{1'}$-O_3 interatomic distances range between 2.563 and 2.857 Å. Thus, all these structural results suggest that the increase in the strength of the hydrogen bond would be responsible for the volume decrease during the phase transition.

Mechanism. We can quantitatively estimate the atoms involved in the transition from the knowledge of the structural distortion vector, $\boldsymbol{\tau}$. This vector is the symmetry-breaking structural distortion of the $P3_121$ phase that leads to the $P3_1$ phase and can be defined as:

$$\tau_{\alpha\kappa} = r_\alpha(\kappa) - r^0_\alpha(\kappa), \quad (1)$$

where $\mathbf{r}(\kappa)$ and $\mathbf{r^0}(\kappa)$ are respectively the position of the κ^{th} atom in the $P3_1$ phase and the corresponding one in the $P3_121$ phase expressed in the setting of the low-symmetry space group. As the origin is undefined in a polar structure, we considered the center of mass of the unit cell as invariant during the transition. This condition represents a shift along the z-direction of 0.0046 in reduced unit of the atomic positions in the $P3_1$ phase. The structural distortion vector is listed in Table 4 and displayed in Figure 5(a). The amplitude of this distortion is defined by the modulus of $\boldsymbol{\tau}$:

$$T = |\boldsymbol{\tau}| = Z \sum_{\alpha,\kappa} \tau^2_{\alpha\kappa}, \quad (2)$$

View Article Online
DOI: 10.1039/D3CP00587A

Sym.	Freq. [cm^{-1}]	Space group	Lattice parameters and angles	Volume [$Å^3$]	ΔE [meV]
A_2	123*i*	$P3_1$	$a = 7.111$ Å, $b = 7.111$ Å, c =13.109 Å $\alpha = 90.00°$, $\beta = 90.00°$, $\gamma = 120.00°$	574.116	-112.98
E	97*i*	C2	$a = 7.126$ Å, $b = 7.142$ Å, $c = 13.127$ Å, $\alpha = 89.34°$, $\beta = 90.00°$, $\gamma = 119.93°$	578.952	-25.04
E	97*i*	P1	a =7.125 Å, $b = 7.126$ Å, $c = 13.119$ Å, $\alpha = 90.32°$, $\beta = 89.26°$, $\gamma = 119.97°$	576.960	-55.34

Table 2 Relaxed lattice parameters, including unit cell volume, and calculated energies ΔE (relative to the $P3_121$ phase and per unit cell) of the different structures obtained from the condensation of each unstable phonon modes in the $P3_121$ phase. The symmetry and frequency of the listed mode is for the $P3_121$ phase.

		Calc.	Exp.			Calc.	Exp.
Lattice parameters							
a (Å)		7.111	7.023(1)	c/a		1.843	1.843
b (Å)		13.109	12.945(1)	Ω_0 ($Å^3$)		574.11	552.89(10)
Atomic positions (reduced units)							
La	x	0.5787	0.5768(1)	H_1	x	0.0814	
	y	0.5659	0.5636(1)		y	0.9889	
	z	0.0056	0.0068(1)		z	0.0024	
O_1	x	0.5180	0.5154(2)	$S_{1'}$	x	0.5535	0.5554(1)
	y	0.3660	0.3651(2)		y	0.5716	0.5711(1)
	z	0.8329	0.8324(1)		z	0.2515	0.2538(1)
O_2	x	0.5898	0.5916(2)	O'_1	x	0.3700	0.3689(2)
	y	0.7310	0.7329(2)		y	0.4865	0.4889(2)
	z	0.8271	0.8254(1)		z	0.1774	0.1807(1)
O_3	x	0.3916	0.3956(2)	$O_{2'}$	x	0.7552	0.7544(2)
	y	0.1436	0.1461(2)		y	0.6411	0.6349(2)
	z	0.0303	0.0287(1)		z	0.1887	0.1893(1)
O_4	x	0.5213	0.5201(2)	$O_{3'}$	x	0.1856	0.1800(2)
	y	0.8894	0.8875(2)		y	0.4243	0.4158(2)
	z	0.0248	0.0240(1)		z	0.9755	0.9776(1)
S_1	x	0.5553	0.5547(1)	O_4'	x	0.8793	0.8786(1)
	y	0.5450	0.5447(1)		y	0.4762	0.4764(1)
	z	0.7612	0.7601(1)		z	0.9939	0.9966(1)
O_{5w}	x	0.9342	0.9344(3)	$H_{1'}$	x	0.9242	
	y	0.9173	0.9148(3)		y	0.0248	
	z	0.9746	0.9763(1)		z	0.9321	
Na	x	0.0065	0.0058(1)				
	y	0.4741	0.4708(1)				
	z	0.1740	0.1750(1)				
Volume of polyhedra P[X] ($Å^3$)							
P[Na]		29.017	27.588	P[La]		33.641	32.567
P[S_1]		1.702	1.649	P[$S_{1'}$]		1.700	1.650
Mean distances (Å)							
Na-O		2.632	2.585	La-O		2.572	2.547
S_1-O		1.492	1.477	$S_{1'}$-O		1.492	1.477
Hydrogen bond distances (Å): O_{5w} – H ··· O							
O_{5w}··· O_2		2.871	2.858(1)	O_{5w}··· $O_{2'}$		2.964	2.974(1)
O_{5w}··· O_3		2.910	2.886(1)	O_{5w}··· $O_{3'}$		3.121	3.047(1)
H_1··· O_3		1.945		H_1··· $O_{2'}$		1.990	
$H_{1'}$··· $O_{2'}$		1.990					

Table 3 Calulated (0 K) and experimental (100 K) structural parameters in the $P3_1$ phase of $NaLa(SO_4)_2.H_2O$. The experimental structure at 100 K is deposited at the Cambridge crystallographic data centre with deposition number: ICSD 2207042.

where Z is the number of formula units (Z =3). We found the the $P3_121$-$P3_1$ transition is accompanied by a distortion whose the amplitude is: $T = 1.72$ Å. In particular, the hydrogen atoms and the atoms labelled O_{5w} contribute by 60% [$= ZA^2_{H_1}/T^2 + ZA^2_{H_{1'}}/T^2$] and 17% [$= ZA^2_{O_{5w}}/T^2$] to this distortion, respectively. The third main contribution is observed for $O_{2'}$-atoms and drops to about 6% only. The contribution of all other atoms remain below 4% each, but represent 17% of the overall distortion. The participation of the sulfur atom labelled S_1 is almost zero. Thus, the structural water and the $O_{2'}$...H hydrogen bonds should drive the $P3_121$–$P3_1$ transition by ~83%.

The phonons involved in the phase transiton can also be identified from the structural distortion vector. Indeed, the set of phonon eigenvectors obtained from the diagonalization of the dynamical matrix in the $P3_121$ phase, $\{\mathbf{e}^j\}_{j=1,...,3\kappa}$, define a complete basis as they satisfy the orthonormalization condition: $\sum_{\alpha\kappa} e^i_{\alpha\kappa} e^j_{\alpha\kappa} = \delta_{ij}$ where i and j are phonon normal modes and δ is the Kronecker symbol. Thus, the structural distortion vector can be decomposed into this basis according to:

$$\tau_{\alpha\kappa} = \sum_j Q_j e^j_{\alpha\kappa}, \tag{3}$$

and the mode amplitude Q_j is then given by:

$$Q_j = \sum_{\alpha\kappa} e^j_{\alpha\kappa} \tau_{\alpha\kappa}. \tag{4}$$

It is also convient to introduce the cosine director, Λ_j, with respect to the distortion direction $\mathbf{e}^j$. Indeed, as by definition $\sum_j \Lambda^2_j$ =1, this quantity better describes the relative contributions of the different normal modes entering into the distortion. In this case, $Q_j = T\Lambda_j$, where T is the distortion amplitude discussed in the previous paragraph. Table 5 reports the dominant contributions ($\Lambda_j > 0.01$) of the normal modes from the $P3_121$ phase to the distortion vector. As expected, the unstable A_2 mode at 123*i* has the highest contributions with a value of Λ =0.694. However, the $P3_1$ phase does not arise from the condensation of this unstable mode only, but also requires the participation of six additional stable modes. Four modes calculated at 123*i*, 49, 79, 97 and 321 cm^{-1} also belong to the A_2 irreducible representation and two modes at 60 and 87 cm^{-1} belong to the A_1 irreducible representation. The contribution of the polar A_2 modes to the distortion represents 85%. These modes are therefore the primary modes and drive

View Article Online
DOI: 10.1039/D3CP00587A

	$\tau_{\alpha\kappa}$			$A_\kappa =$
κ	$\alpha = x$	$\alpha = y$	$\alpha = z$	$[\sum_\alpha \tau^2_{\alpha\kappa}]^{1/2}$
La	0.0972	0.0099	0.0141	0.099
	(0.0144)	(0.0016)	(0.0011)	
O_1	0.1552	0.0475	0.0114	0.163
	(0.0255)	(0.0077)	(0.0009)	
O_2	-0.0946	-0.0184	0.0204	0.099
	(-0.0147)	(-0.0030)	(0.0016)	
O_3	-0.066	-0.1145	-0.0524	0.142
	(-0.0185)	(-0.0185)	(-0.0040)	
O_4	0.1097	0.0385	0.0634	0.132
	(0.0185)	(0.0062)	(0.0048)	
S_1	-0.0109	0.0151	0.0094	0.021
	(-0.0003)	(0.0024)	(0.0007)	
O_{5w}	0.1005	-0.0349	-0.3936	0.408
	(0.0112)	(-0.0056)	(-0.0300)	
Na	0.0621	-0.0268	0.0364	0.077
	(0.0065)	(-0.0043)	(0.0028)	
H_1	0.0304	0.2265	-0.4272	0.485
	(0.0226)	(0.0366)	(-0.0325)	
$S_{1'}$	0.0215	0.0992	0.0377	0.108
	(0.0110)	(0.0160)	(0.0029)	
$O_{1'}$	0.1053	-0.0370	0.0045	0.112
	(0.0117)	(-0.0060)	(0.0003)	
$O_{2'}$	0.0213	0.2260	0.0675	0.237
	(0.0212)	(0.0365)	(0.0051)	
$O_{3'}$	0.11800	0.0874	0.0086	0.147
	(0.0236)	(0.0141)	(0.0007)	
$O_{4'}$	0.0678	-0.1649	0.0628	0.189
	(-0.0038)	(-0.0266)	(0.0048)	
$H_{1'}$	-0.0787	-0.2109	-0.5534	0.598
	(-0.0281)	(-0.0341)	(-0.0421)	

Table 4 Calculated atomic structural distortion vector ($\boldsymbol{\tau}$) of the $P3_1$ phase with respect to the $P3_121$ phase in $NaLa(SO_4)_2.H_2O$. This distortion has been calculated considering the center of mass as invariant. Only atoms of the asymmetric unit are listed. All data are in Cartesian coordinates (Å) except the data between brackets which are in reduced units. A_κ is the partial atomic modulus satisfying $T = Z\sum_\kappa A^2_\kappa$.

Symmetry	Frequency [cm^{-1}]	Λ_j
A_2	$123i$	0.694
A_2	49	0.549
A_1	60	0.207
A_2	79	-0.153
A_1	87	0.299
A_2	97	-0.160
A_2	321	0.120

Table 5 Contributions Λ_j (see text) of the phonon modes j to the distortion linking the $P3_121$ and the $P3_1$ structures in $NaLa(SO_4)_2.H_2O$. Only contributions higher than 0.01 are listed.

the transition. They are also responsible of the polar character of the transition. This polarization can be roughly estimated as:

$$P_\alpha = \frac{1}{\Omega_0}\sum_{\beta\kappa} Z^*_{\alpha\beta}(\kappa)\tau_{\beta\kappa}, \quad (5)$$

where Z^* is the Born effective charge tensor of atom κ. We found P_z =1.3 μC.cm^{-2} using the Born effective charges of the $P3_121$ phase, which is quite small compared to standard ferroelectric material like $BaTiO_3$ ($\sim 26\mu.cm^{-2}$)[38]. The two modes belonging to the fully symmetric A_1 irreducible representation contribute by 13% to the distortion. These modes do not break the symmetry of the $P3_121$ phase but contribute to the distortion by symmetry (von Neumann principle). They are therefore qualified of secondary modes and are only induced by the presence of the primary A_2 modes. All modes with A_2 or A_1 symmetry, and other than those listed in table 5, represent an overall participation of 2% to the distortion.

The infrared spectroscopy should provide an experimental evidence of this nonpolar–polar $P3_121$–$P3_1$ phase transition.

4.3 Independent experimental confirmation of the $P3_121$–$P3_1$ phase transition

The temperature dependence of the infrared responses in $NaLa(SO_4)_2.H_2O$ has been recorded between 25 and 295 K. Figures 6 and 7 display the far-infrared (50–580 cm^{-1}) and the mid-infrared (580–3700 cm^{-1}) spectral region, respectively. The domain between 1800 and 3000 cm^{-1} has been relegated in Supplementary information (Figure S1) as is not relevant for the present discussion. This domain reports bands with weak intensities assigned to combination modes of sulphate groups.

The infrared modes within the 50–1800 cm^{-1} range show a monotonous dependence with a quasi-harmonic behaviour between 295 and 200 K. From this temperature, we observe the appearance of additional several bands which are increasingly better resolved down to 25 K. They are centered at 25 K about 1150, 1086, 545, 523, 488, 470, 450, 235, 214, 185, 160, 137 and 76 cm^{-1}. The appearance of these bands highlights that $NaLa(SO_4)_2.H_2O$ undergoes a phase transition at 200 K from the nonpolar $P3_121$ space group to a polar space group. X-ray diffraction has been performed at 100 K on a single crystal to identify this polar space group. Our refinement showed that the group in question was indeed the one predicted by our DFT calculations,

View Article Online
DOI: 10.1039/D3CP00587A

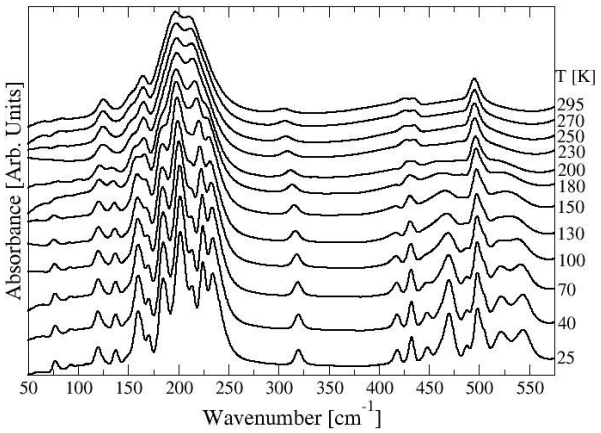

Fig. 6 Temperature dependence of the far-infrared modes in $NaLa(SO_4)_2.H_2O$ recorded between 295 and 25 K.

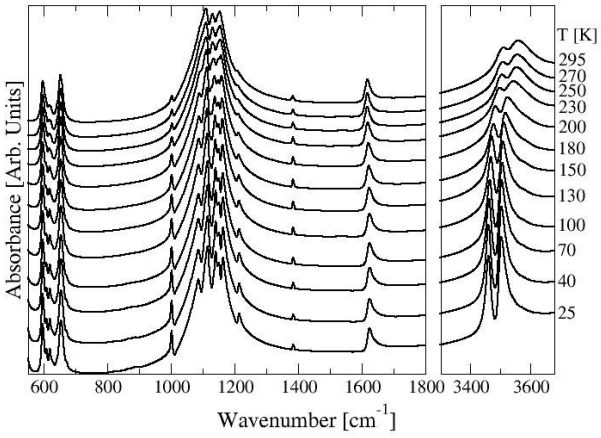

Fig. 7 Temperature dependence of the mid-infrared modes in $NaLa(SO_4)_2.H_2O$ recorded between 295 and 25 K.

namely the $P3_1$ space group. Details of the data collection are summarized in Table S1 (ESI). This observed phase transition was found to be reversible by infrared spectroscopy and x-ray diffraction.

By reducing the symmetry of the $P3_121$ phase, the number of irreducible representations is also reduced. The correlation table between the D_3 and C_3 point group shows that the A_1 and A_2 irreducible representations in the $P3_121$ phase turn to be an unique A representation in the $P3_1$ phase. This A-representation is now both infrared and Raman active. Thus, the origin of the infrared additional bands previously discussed is correlated to the Raman A_1-modes in the $P3_121$ phase which are now active with A-symmetry in the $P3_1$ phase.

The calculated infrared spectra of the $P3_1$ phases is displayed in Figure 8. The irreducible representation of the optical phonon modes can easily be derived from the $P3_121$ phase as: $\Gamma_{opt} = 44A \oplus 44E$. Each atom of the asymmetric unit contributes by $3A \oplus 3E$. The infrared spectra are dominated within the 3200–3700 cm^{-1} range by a doublet located about 3528 cm^{-1} at room temperature. This doublet is assigned to the O-H stretching modes and undergoes a strong softening in frequency ($\sim$45 cm^{-1}) with decreasing the temperature. This redshift is the fingerprint of interatomic O...H hydrogen bonds as a decrease in the intramolecular O-H force constants is expected when the intermolecular O...H hydrogen bonds are subjected to low temperature[39]. This suggests a reinforcement of the hydrogen bonds in the $P3_1$ phase in agreement with our DFT prediction.

Structural parameters of the phase solved in the $P3_1$ space group by x-ray diffraction are listed in Table 3 and compared with the ones from the DFT calculation. Data collection and refinement details are given in supporting information (Tables S1 to S5). The relative error is about +1.3% in the lattice parameters for each direction. The calculated c/a ratio is in perfect agreement with the experiment. The experiment shows that the unit cell volume in the $P3_1$ phase is slightly smaller (-0.9%) than in the $P3_121$ phase in agreement with the DFT results. This small difference is coherent with a phase transition at the Brillouin zone center. Although the experimental position of hydrogen atoms could not be determined, we can still get a distortion vector from the experimental positions between the $P3_1$ and the $P3_121$ structures according to Eq. (1). We get an experimental distortion amplitude of T^{exp} =0.96 Å without the consideration of hydrogen atoms. This value is in good agreement with the calculated distortion amplitude (T^{calc} =1.08 Å) without hydrogen atoms (against T^{calc} =1.72 Å including hydrogen atoms). The experimental distortion vector (Figure 5(c)) agrees well with the DFT calculations (Figure 5(b)), which indicates that the experimental and the calculated $P3_1$ structures are very close. The water oxygen atoms (O_{5w}) dominate the distortion.

4.4 Piezoelectric properties of the $P3_1$ phase

This section is purely theoretical as piezoelectric measurements were not possible due to the small size of our single crystals.

In the C_3-point group, the piezoelectric-stress tensor has six independent nonzero elements[40], namely e_{11}, e_{12}, e_{13}, e_{33}, e_{41} and

View Article Online
DOI: 10.1039/D3CP00587A

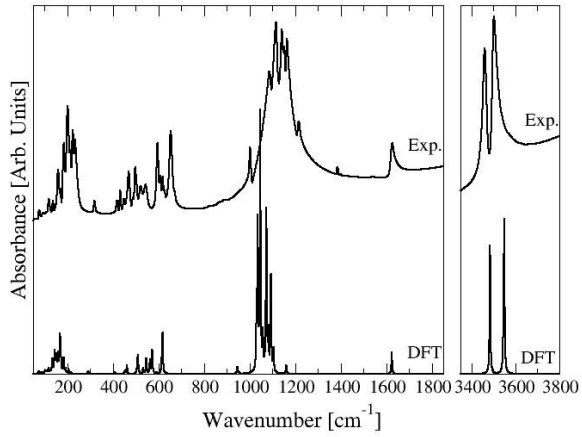

Fig. 8 Experimental infrared absorbance spectrum of $NaLa(SO_4)_2.H_2O$ in the $P3_1$ phase (25 K) and the corresponding calculated spectrum (0 K). The calculated spectrum is displayed using a Lorentzian line shape and a constant linewidth fixed at 2 cm^{-1}.

	11	12	13	33	41	51
Piezoelectric-stress (C/m^2)						
$e^{el}_{j\alpha}$	-0.024	-0.004	0.014	-0.013	0.016	0.015
$e^{ph}_{j\alpha}$	0.075	-0.135	-0.141	-0.113	-0.077	-0.052
$e_{j\alpha}$	0.051	-0.139	-0.127	-0.126	-0.061	-0.037
Piezoelectric-strain (pC/N)						
$d_{j\alpha}$	1.40	-3.25	-0.98	-0.83	-3.42	-1.16

Table 6 Calculated independent elements of the piezoelectric-stress and piezoelectric-strain tensors in the $P3_1$ phase of $NaLa(SO_4)_2.H_2O$. The piezoelectric-stress ($e = e^{el} + e^{ph}$) has been decomposed into an electronic (e^{el}) and a vibrational (e^{ph}) contribution. By symmetry with have the following relations: $e_{11} = -e_{12} = -e_{62}$, $e_{12} = -e_{22} = e_{61}$, $e_{41} = -e_{52}$, $e_{51} = e_{42}$ and $e_{13} = e_{23}$.

e_{51}. They have been calculated in the zero Kelvin limit and are listed in Table 6. We observe that the absolute values of e_{11}, e_{41} and e_{51} are between 0.037 and 0.061 C/m^2, which is similar to the values measured for e_{41} in α-quartz[2,41] (0.04-0.06 C/m^2). The highest piezoelectric-stress values are observed for the e_{12}, e_{13} and e_{33} elements. Their absolute values are very close and reach 0.139 C/m^2 for e_{12}. This value is similar to that observed in α-quartz[2] (e_{11} ~0.14-0.17 C/m^2) and α-quartz-type $AlPO_4$[1,42] with e_{11} =0.16 C/m^2. However, we are still quite far of the measured values in the langasites such as $La_3Ga_5SiO_{14}$ with[43] e_{11} =0.44 C/m^2 or the theoretical values predicted[19] in $BaZnO_2$ (e_{11} =0.72 C/m^2).

The decomposition of the piezoelectric-stress elements into an electronic (e^{el}) and a phonon-mediated (e^{ph}) contribution is also reported in Table 6. These two contributions have the same magnitude and opposite sign in the case of the e_{11}, e_{41} and e_{51} elements, yielding to small overall values. For the e_{13} and e_{33} elements, the electronic contribution is one order smaller in magnitude than the vibrational one. For the e_{12} element, the electronic contribution is almost zero. Thus, the vibrational contribution strongly dominates the e_{12}, $e_{13}$and e_{33} piezoelectric-stress response. In particular, phonon modes belonging to the E-irreducible representation govern the e_{12} and e_{13} responses whereas phonon modes belonging to the A representation are at the origin to the e^{ph}_{33} response. An inspection of the calculated polarity and strain coupling for each phonon mode shows that all modes belonging to a same irreducible representation contribute without strong dominance.

The phonon-mediated contribution can also be analyzed from the polyhedron representation. The contribution of each independent polyhedron P(X) to e^{ph} has been estimated as[44]:

$$e^{ph}_{j\alpha}[P(X)] = e^{ph}_{j\alpha}(X) + \frac{1}{f}\sum_{O\in P(X)} e^{ph}_{j\alpha}(O), \quad (6)$$

where X ={La, Na, S_1, $S_{1'}$} and f is an integer number given the number of polyhedra sharing the same oxygen atom. This number is equal to 3 for all oxygen except the water oxygens where f =2. We do not consider that the water molecules are included in the P(La) polyhedra. Thus, their contributions are given by:

$$e^{ph}_{j\alpha}[water] = \frac{1}{2}e^{ph}_{j\alpha}(O_{5w}) + e^{ph}_{j\alpha}(H_1) + e^{ph}_{j\alpha}(H_{1'}). \quad (7)$$

The atom-contribution, $e^{ph}_{j\alpha}(\kappa)$, of a κ-atom in the unit cell is obtained according to[44]:

$$e^{ph}_{j\alpha}(\kappa) = \frac{1}{\Omega_0}\sum_{\beta} Z^*_{\alpha\beta}(\kappa)\frac{du_\beta(\kappa)}{d\eta_j} \quad (8)$$

where $du/d\eta$ is the displacement-response internal-strain that describes the first-order displacements resulting from a first-order strain. Results of this projection are shown in Table 7 for the independent elements of $e_{j\alpha}$ whose the values are the highest. We do not observe a clear dominance of the polyhedral contributions for e^{ph}_{12}. However, their sign shows that the P($S_{1'}$) polyhedra lead to decrease the overall piezoelectric response. In contrast to e^{ph}_{12}, the P(La) and P(S_1) polyhedra dominate e^{ph}_{13}. Their share the same sign, which is the most favorable situation. The polyhedra centered on the sulfur atoms dominate e^{ph}_{33}. However, the situation is less favorable than in the previous case as the P($S_{1'}$) response is counterbalanced in part by the P(S_1) polyhedra. The piezoelectric response of the structural water is small (~0.02-0.04 C/m^2) and it does not contribute to significatively increase an element of the piezoelectric-stress tensor.

In contrast to the piezoelectric-stress, the knowledge of the piezoelectric-strain is more suitable for potential applications. For example, this quantity estimates the magnitude of the piezoelectric response in an actuator. It can be calculated as:[45],

$$d_{j\alpha} = \sum_k S^{(\mathscr{E})}_{jk} e_{k\alpha} \quad (9)$$

where $S^{(\mathscr{E})}$ is the elastic compliance tensor defined under the condition of fixed (vanishing) electric field. The full elastic tensor in the $P3_1$ phase has seven independent elastic constants: $C^{(\mathscr{E})}_{11}$, $C^{(\mathscr{E})}_{12}$,

View Article Online
DOI: 10.1039/D3CP00587A

Polyhedron	e_{12}^{ph}	e_{13}^{ph}	e_{33}^{ph}
P(La)	-0.046	-0.071	-0.056
P(Na)	-0.098	+0.0356	-0.0225
$P(S_1)$	-0.036	-0.101	+0.2385
$P(S_{1'})$	+0.083	-0.026	-0.309
water	-0.038	+0.022	+0.036

Table 7 Calculated vibrational contribution (e^{ph}) of each polyhedron P(X) in the $P3_1$ phase of $NaLa(SO_4)_2.H_2O$. Values are given in C/m^2. P(X) is the polyhedron centered on the X-atom (see text). Water labels the strutural water.

Index	$C^{(\mathscr{E})}$ (GPa)	$S^{(\mathscr{E})}$ (TPa^{-1})
11	73.78	17.73
12	30.57	-5.75
13	29.42	-4.25
14	2.32	-2.49
15	1.20	-1.29
33	82.89	15.08
44	21.86	44.43

Table 8 Calculated elastic ($C^{(\mathscr{E})}$) and compliance ($S^{(\mathscr{E})} = [C^{(\mathscr{E})}]^{-1}$) constants defined under the condition of fixed (vanishing) electric field in the $P3_1$ phase of $NaLa(SO_4)_2.H_2O$.

$C_{13}^{(\mathscr{E})}$, $C_{14}^{(\mathscr{E})}$, $C_{15}^{(\mathscr{E})}$, $C_{33}^{(\mathscr{E})}$ and $C_{44}^{(\mathscr{E})}$. These constants are listed in Table 8 and satisfy the Born stability inequalities[46] for the trigonal space group, which indicates that this structure is mechanically stable. The independent elements of the piezoelectric-strain tensor are listed in Table 6. The consideration of the elastic compliances changes most of the tendencies previously discussed on the piezoelectric-stress tensor. Indeed, the highest values (∼3.3 pC/N) of the piezoelectric-strain are now observed for the (1,2) and (1,4)-elements. The high value of d_{14} is related to the high value of S_{44}. The value of the other independent elements are about 1 pC/N. The shear d_{41} value is about five times higher than that measured on α-quartz ($d_{41} = 0.73$ pC/N)[2] or predicted on $BaZnO_2$ ($d_{41} \sim 0.67$ pC/N)[19]. However, this value is similar with that reported on the $La_3Ga_5SiO_{14}$ lagasite[16] ($d_{41} \sim 4.5$ pC/N). The d_{22} value cannot be compared to these coumpounds as it is zero by symmetry in a 32-point group. However, we can compared to the d_{11} which is also a longitudinal mode. The d_{22} value of the $P3_1$ phase in $NaLa(SO_4)_2.H_2O$ is slightly higher than in α-quartz ($d_{11} = 2.31$ pC/N)[2] but about twice smaller than in lagasite[16] ($d_{11} \sim 6.5$ pC/N). We are also far from the predictions for $BaZnO_2$ ($d_{11} = 11.84$ pC/N)[19].

5 Conclusions

In this article, we reported the existence in $NaLa(SO_4)_2.H_2O$ of a displacive phase transition at 200 K from the nonpolar $P3_121$ to the polar $P3_1$ space groups combining first based calculations and experiments (infrared spectroscopy and x-ray diffraction). Our calculations highlighted the existence of two distinct unstable phonon modes in this $P3_121$ space group. The condensation of these unstable mode allows to determine the phase transitions toward the compatible subgroups using symmetry considerations. Among them, we identified the polar $P3_1$ as the most probable subgroup according to energy criterion. Then, infrared spectroscopy and x-ray diffraction experiments supported these predictions. Infrared measurements showed the existence of a phase transition at 200 K and the $P3_1$ space group was identified by x-ray diffraction. The mechanism of this phase transition has been explained from symmetry-adapted distortion modes. The structural water and hydrogen bonding are the mechanism driven the phase transition. The A_2 polar irreducible representation is the primary order parameter. This representation is also responsible of the polar character of the transition.

The piezoelectric properties of this new $P3_1$ phase have been investigated by first principles based calculations. The six independent piezoelectric-stress constants (e_{11}, e_{12}, e_{13}, e_{33}, e_{41} and e_{51}) have been calculated. The highest piezoelectric-stress values are observed for the e_{12}, e_{13} and e_{33} with about -0.13 C/m^2. We discussed microscopic origin of these constants from the analysis of their electronic and the vibrational contributions. We found that the phonon-mediated contribution is the dominant contribution. The vibrational contribution has been also analyzed from the contribution of the different polyhedra used as building blocks in the $NaLa(SO_4)_2.H_2O$ structure. The elastic compliance tensors have been calculated and we derived the piezolectric-strain constants. The highest values in the zero Kelvin limit are predicted for d_{12} and d_{41} with ∼3.4 pC/N. These values are between those observed in α-quartz and α-$GaPO_4$ which is commonly used in piezoelectricity. Thus, $NaLa(SO_4)_2.H_2O$ could be a potential candidate for piezoelectric application in the low temperature range (below 200 K).

Conflicts of interest

There are no conflicts to declare.

Acknowledgements

Infrared experiments were performed on the IR-Raman technological platform of the University of Montpellier.

Notes and references

1 E. Philippot, D. Palmier, M. Pintard, A. Goiffon. A general survey of quartz and quartz-like materials: Packing distortions, temperature, and pressure effects. *J. Solid State Chem.*, 1996, **123**, 1-13.

2 R. Bechmann. Elastic and piezoelectric constants of alpha-quartz. *Phys. Rev.*, 1958, **110**, 1060-1061.

3 W. Heywang, K. Lubitz, W. Wersing. Piezoelectricity, Evolution and Future of a Technology; Springer, Springer-Verlag Berlin Heidelberg, 2008.

4 H. Grimm, B. Dorner. On the mechanism of the $\alpha - \beta$ phase transformation of quartz. *J. Phys. Chem. Solids*, 1975, **36**, 407-413.

5 J. Haines, O. Cambon, R. Astier, P. Fertey, C. Chateau. Crystal Structures of α-Quartz Homeotypes Boron Phosphate and Boron Arsenate: Structure–Property Relationships. *Z. Kristallogr.*, 2004, **219**, 32-37.

View Article Online
DOI: 10.1039/D3CP00587A

6 J. C. Jumas, A. Goiffon, B. Capelle, A. Zarka, J. C. Doukhan, J. Schwartzel, J. Détaint, E. Philippot. Crystal Growth of Berlinite, $AlPO_4$: Physical Characterization and Comparison with Quartz. *J. Crystal Growth*, 1987, **80**, 133-148.

7 O. Cambon, P. Yot, D. Balitsky, A. Goiffon, E. Philippot, B. Capelle, J. Détaint. Crystal Growth of $GaPO_4$: A Very Promising Material for BAW Devices Manufacturing. *Ann. Chim. Sci. Mat.*, 2001, **26**, 79-84.

8 E. Philippot, A. Ibanez, A. Goiffon, M. Cochez, A. Zarka, B. Capelle, J. Schwartzel, J. Détaint. A Quartz-Like Material: Gallium Phosphate ($GaPO_4$); Crystal Growth and Characterization. *J. Crystal Growth*, 1993, **130**, 195-208.

9 O. Cambon, G. M. Bhalerao, D. Bourgogne, J. Haines, P. Hermet, D. A. Keen, M. G. Tucker. Vibrational Origin of the Thermal Stability in the High-Performance Piezoelectric Material $GaAsO_4$. *J. Am. Chem. Soc.*, 2011, **133**, 8048-8056.

10 P. Hermet, J. Haines, J.-P. Aubry and O. Cambon. Origin and Mechanism of Piezoelectricity in α-Quartz-type $M^{III}X^{V}O_4$ Compounds (M = B, Al, or Ga; X = P or As). *J. Phys. Chem. C*, 2016, **120**, 26645-26651.

11 M. Souleiman, P. Hermet, A. Haidoux, C. Levelut, J. Haines and O. Cambon. Combined Experimental and Theoretical Raman Scattering Studies of α-Quartz-Type $FePO_4$ and $GaPO_4$ End Members and $Ga_{1-x}Fe_xPO_4$ Solid Solutions. *RSC Advances*, 2013, **3**, 22078.

12 J. Nosek, M. Pustka. Determination of the Electromechanical Coupling Factor of Gallium Orthophosphate ($GaPO_4$) and its Influence on Resonance-Frequency Temperature Dependencies. *IEEE transactions, Ferroelectrics and frequency control*, 2006, **53**, 10-14.

13 P. Fertey, P. Alle, E. Wenger, B. Dinkespiler, O. Cambon, J. Haines, S. Hustache, K. Med-joubi, F. Picca, A. Dawiec, P. Breugnon, P. Delpierre, C. Mazzoli, C. Lecomte. Diffraction Studies Under In-Situ Electric Field Using a Large-Area Hybrid Pixel XPAD Detector. *J. Appl. Cryst.*, 2013, **46**, 1151-1161.

14 E. Philippot, P. Armand, P. Yot, O. Cambon, A. Goiffon, G. J. McIntyre, P. Bordet. Neutron and X-Ray Structure Refinements Between 15 and 1073 K of Piezoelectric Gallium Arsenate, $GaAsO_4$: Temperature and Pressure Behavior Compared with Other α-Quartz Materials. *J. Solid State Chem.*, 1999, **146**, 114-123.

15 B. Boutahraoui, E. A. Ghezal, A. Nehari, K. Zaidat, M. Allani, H. Cabane, M. Dumortier, I. Gerasymov, O. Sidletskiy, S. Obbade, L. Jouffret, K. Lebbou. Impact of growth atmosphere on langatate ($La_3Ga_{5.5}Ta_{0.5}O_{14}$) crystals grown by czochralski technique and its coloration. *Optical Materials*, 2022, **128**, 112409.

16 D. Irzhak and D. Roshchupkin. Measurement of independent piezoelectric moduli of $Ca_3NbGa_3Si_2O_{14}$, $La_3Ga_{5.5}Ta_{0.5}O_{14}$ and $La_3Ga_5SiO_{14}$ single crystals. *J. Appl. Cryst.*, 2018, **51**, 1174-1181.

17 J. Bohm, R. B. Heimann, M. Hengst, R. Roewer, J. Schindler. Czochralski growth and characterization of piezoelectric single crystals with langasite structure: $La_3Ga_5SiO_{14}$ (LGS), $La_3Ga_{5.5}Nb_{0.5}O_{14}$ (LGN), and $La_3Ga_{5.5}Ta_{0.5}O_{14}$ (LGT) Part I. *J. Crystal Growth*, 1999, **204** 128-136.

18 A. A. Kaminskii, B. V. Mill, G. G. Khodzhabagyan, A. F. Konstantinova, A. I. Okorochkov, I. M. Silvestrova. Investigation of trigonal $(La_{1-x}Nd_x)_3Ga_5SiO_{14}$ crystals. I. Growth and optical Properties. *Phys. Stat. Sol. (a)*, 1983, **80**, 387.

19 Y. Zeng, Y. Zheng, J. Xin, E. Shi. First-principle study the piezoelectricity of a new quartz-type crystal $BaZnO_2$. *Comput. Mater. Sci.*, 2012, **56**, 169-171.

20 H. G. Vonschnering, R. Hoppe, J. Zemann. Die Kristallstruktur des $BaZnO_2$. *Z. Anorg. Allg. Chem.*, 1960, **305**, 241-254.

21 O. Lindgren. The Crystal Structure of Sodium Cerium(III) Sulfate Hydrate, $NaCe(SO_4)_2.H_2O$. *Acta Chem. Scand.*, 1977, **31**, 591-594.

22 C.-D. Wu, Z.-Y. Liu. Hydrothermal synthesis of a luminescent europium(III) sulfate with three-dimensional chiral framework structure. *J. Solid State Chem.*, 2006, **179**, 3500-3504.

23 B. Zhai, Z. Li, C. Zhang, F. Zhang, X. Zhang, F. Zhang, G. Cao, S. Li, X. Yang. Three rare Ln–Na heterometallic 3D polymers based on sulfate anion: Syntheses, structures, and luminescence properties. *Inorg. Chem. Commun.*, 2016, **63**, 16-19.

24 J. Perles, C. Fortes-Revilla, E. Gutiérrez-Puebla, M. Iglesias, M. A. Mongé, C. Ruiz-Valero, N. Snejko. Synthesis, Structure, and Catalytic Properties of Rare-Earth Ternary Sulfates. *Chem. Mater.*, 2005, **17**, 2701-2706.

25 A. K. Paul, R. Kanagaraj. Synthesis, Characterization, and Crystal Structure Analysis of New Mixed Metal Sulfate $NaPr(SO_4)_2(H_2O)$. *J. Struct. Chem.*, 2019, **60**, 477-484.

26 A. C. Blackburn, R. E. Gerkin. Sodium lanthanum(III) sulfate monohydrate, $NaLa(SO_4)_2.H_2O$. *Acta Crystallogr.*, 1994, **50**, 835-838.

27 A. C. Blackburn, R. E. Gerkin. Redetermination of sodium cerium(III) sulfate monohydrate, $NaCe(SO_4)_2.H_2O$. *Acta Crystallogr.*, 1995, **51**, 2215-2218.

28 Ö. Kolcu, B. Zümreoğlu-Karan. Nonisothermal Dehydration Kinetics of Sodium-Light Lanthanoid Double Sulfate Monohydrates. *Thermochim. Acta*, 1997, **296**, 135-139.

29 Ö. Kolcu, B. Zümreoğlu-Karan, B. Thermal Properties of Sodium-Light-Lanthanoid Double Sulfate Monohydrates. *Thermochim. Acta*, 1994, **240**, 185-198.

30 H. Azeroual, L. Vendier, A. Geneste, D. Granier, L. Alvarez, P. Hermet and O. Cambon. $NaLa(SO_4)_2.H_2O$ thermal conversion and $Na_3La(SO_4)_3$ crystal growth. *J. Solid State Chem.*, 2023, **317**, 123570.

31 X. Gonze, B. Amadon, P. M. Anglade, J. M. Beuken, F. Bottin, P. Boulanger, F. Bruneval, D. Caliste, R. Caracas, *et al.* ABINIT: First-principles Approach to Material and Nanosystem Properties. *Comput. Phys. Comm.*, 2009, **180**, 2582-2615.

32 J. P. Perdew, K. Burke and M. Ernzerhof. Generalized Gradient Approximation Made Simple. *Phys. Rev. Lett.*, 1996, **77**, 3865-3868.

33 H. J. Monkhorst and J. D. Pack. Special Points for Brillouin-Zone Integrations. *Phys. Rev. B*, 1976, **13**, 5188-5192.

34 P. Hermet, J.-L. Bantignies, A. Rahmani, J.-L. Sauvajol, M. R. Johnson and F. Serein. Far- and Mid-Infrared of Crystalline

View Article Online
DOI: 10.1039/D3CP00587A

2,2'-Bithiophene: Ab Initio Analysis and Comparison with Infrared Response. *J. Phys. Chem. A*, 2005, **109**, 1684-1691.

35 G. Bergerhoff, M. Berndt, K. Brandenburg and T. Degen. Concerning Inorganic Crystal Structure Types. *Acta Cryst. B*, 1999, **55**, 147-156.

36 $\Delta = 0$ when two structures are identical.

37 G. Herzberg. Infrared and Raman Spectra of Polyatomic Molecules. Ed. Van Nostrand (1945).

38 H. H. Wieder. Electrical Behavior of Barium Titanate Single Crystals at Low Temperatures. *Phys. Rev.*, 1955, **99**, 1161-1165.

39 R. Leparc, V. T. Freitas, P. Hermet, A. M. Cojocariu, X. Cattoën, H. Wadepohl, D. Maurin, C. H. Tse, J. R. Bartlett, R. A. S. Ferreira, L. D. Carlos, M. Wong Chi Man and J.L. Bantignies. Infrared and Raman spectroscopy of Non-conventional Hydrogen Bonding Between N,N'-Disubstituted Urea and Thiourea Groups: a Combined Experimental and Theoretical Investigation. *Phys. Chem. Chem. Phys*, 2019, **21**, 3310-3317.

40 IEEE Standard on Piezoelectricity, ANSI/IEEE Std. 176-1978, New IEEE (1978).

41 R. Tarumi, K. Nakamura, H. Ogi, M. Hirao. Complete set of elastic and piezoelectric coefficients of α-quartz at low temperatures. *J. Appl. Phys.*, 2007, **102**, 113508.

42 D. S. Bailey, J. C. Andle, D. L. Lee, W. Soluch, J. F. Vetelino, B. H. T. Chai. in *Proceedings of the 1983 IEEE Ultrasonics Symposium* (IEEE, New York, 1983) pp. 335-340.

43 R. C. Smythe and E. Hague. Determination of the piezoelectric constants of LGN, LGS & LGT. International Frequency Control Symposium, 2000, pp. 191-194.

44 P. Hermet. Piezoelectric Response in α-Quartz-Type GeO_2. *J. Phys. Chem. C*, 2016, **120**, 126-132.

45 X. Wu, D. Vanderbilt and D. R. Hamann. Systematic Treatment of Displacements, Strains, and Electric Fields in Density-Functional Perturbation Theory. *Phys. Rev. B*, 2005, **72**, 035105.

46 H. Ozisik, K. Colakoglu, H. B. Ozisik and E. Deligoz. Structural, Elastic, and Lattice Dynamical Properties of Germanium Diiodide (GeI_2). *Comput. Mater. Sci.*, 2010, **50**, 349-355.